Investigation of the Structural and Optical Properties of Zinc Ferrite Nanoparticles Synthesized via a Green Route

Jayant K. Jogi[1] · S. K. Singhal[1] · Ravindra Jangir[2] · Abhilash Dwivedi[3] · Ashish R. Tanna[4] · Rashmi Singh[5] · Minal Gupta[6] · Pankaj R. Sagdeo[6]

Abstract

We report herein the synthesis of $ZnFe_2O_4$ (ZF) nanoparticles via a simple and eco-friendly green route using lemon juice as a reducing agent and fuel. The effect of different calcination temperatures on the particle size and bandgap of grown ZF nanoparticles was investigated. The structural, morphological and optical properties of the synthesized nanoparticles were evaluated using synchrotron x-ray diffraction (S-XRD), field emission scanning electron microscopy (FE-SEM) and UV-visible diffuse reflectance spectroscopy (UV-Vis-DRS), respectively. S-XRD confirmed a spinel F-d3m phase in all four samples calcined at 350°C, 550°C, 750°C and 1000°C. The crystallite size calculated from the Debye–Scherrer equation showed an increase from 14 nm to 20 nm with the increase in calcination temperature. Williamson–Hall (W-H) analysis revealed an increase in the particle size from 16 nm to 21 nm and a decrease in the lattice microstrain from 0.913×10^{-3} to 0.154×10^{-4} with the increase in calcination temperature. The optical bandgap of the ZF nanoparticles obtained from UV-Vis-DRS decreased from 2.265 eV to 2.225 eV with the increase in calcination temperature. The ZF nanoparticles with tunable particle size, lattice microstrain and optical bandgap have potential application in ferrofluid, electromagnetic shielding, photocatalysis, hyperthermia, dye degradation and other areas.

✉ S. K. Singhal
  s_k_singhal@yahoo.co.uk

1   Department of Science and Humanities, Lukhdhirji Engineering College (Affiliated to Gujarat Technological University, Ahmedabad), Morbi, Gujarat, India

2   Synchrotron Utilization Section, Raja Ramanna Centre for Advance Technology, Indore, Madhya Pradesh, India

3   High Pressure and Synchrotron Radiation Physics Division, Bhabha Atomic Research Centre, Mumbai, Maharashtra, India

4   Department of Physics, RK University, Rajkot, Gujarat, India

5   Laser Section, Raja Ramanna Centre for Advance Technology, Indore, Madhya Pradesh, India

6   Material Research Laboratory, Department of Physics, Indian Institute of Technology, Indore, Madhya Pradesh, India

Introduction

Nanomaterials are garnering increasing attention in comparison to bulk materials because of their enhanced surface-to-volume ratio and quantum phenomena.[1] Metal ferrites are described as MFe_2O_4 where M^{2+} is a valance metal ion such as Zn^{2+}, Cu^{2+}, Mg^{2+}, Co^{2+}, or Ni^{2+}. $ZnFe_2O_4$ (ZF) is a more versatile material than other metal ferrites because of its excellent superparamagnetic, electrical, magnetic and biomedical properties.[2] Metal ferrites have numerous applications in the fields of ferrofluid technology and spintronic devices,[3] microelectronic sensors,[4] desulfurization sorbent for coal gas,[5] electromagnetic shielding,[6] photocatalysis and dye degradation,[4,7] hyperthermia,[8] COVID-19 detection,[9] drug delivery,[10] in vitro destruction of cancer cells by near-infrared (NIR) laser irradiation in the presence of a magnetic field,[11] water splitting in the presence of sunlight[12] and electromagnetic equipment in the radio-frequency region, as ZF not only has greater electrical resistivity, but its permeability
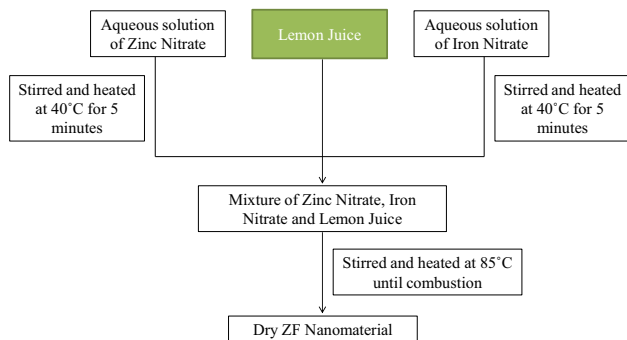
is also frequency-dependent.[13, 14] In $ZnFe_2O_4$, oxygen atoms form face-centered cubic (FCC) packing, while Fe and Zn occupy octahedral and tetrahedral sites, respectively. A unit cell of a spinel structure consists of a total of 64 sites contributed from eight FCC cells, out of which 56 sites are occupied and the remaining eight sites are vacant. Depending on how Zn ions occupy different interstices, a spinel structure can be normal or inverse spinel. One unit cell consists of eight molecules of $ZnFe_2O_4$ or 56 ions out of which eight are Zn^{2+}, 32 are O^{2-} and 16 are Fe^{3+}. All tetrahedral (A-site) interstitial positions are occupied by Zn^{2+} ions, and all octahedral (B-site) interstitial positions are occupied by Fe^{3+} in the normal spinel structure of $ZnFe_2O_4$, while half of Fe^{3+} ions occupy tetrahedral and the other half of Fe^{3+} and all Zn^{2+} ions occupy octahedral sites in an inverse spinel structure. The structural, optical and electrical properties are determined by Zn ion distribution between tetrahedral and octahedral sites, while its magnetic properties depend on individual particles and its environment. The size and shape of ZF nanoparticles depend on the synthesis route and calcination temperature. There are many methods to synthesize ZF nanoparticles and its composites, including sol–gel,[15] micro-emulsion,[16] sonochemical,[17] microwave,[18] solid state[19,20] co-precipitation,[21] high-energy ball milling,[22] and green routes.[23,24,25,18] ZF composites, spherical in shape and with diameters ranging from 5 nm to 25 nm at calcination temperatures of 500°C and 700°C, were obtained when *Moringa oleifera* (bael) extract was dissolved in a mixture of ferric(III) nitrate nonahydrate and zinc nitrate hexahydrate under magnetic stirring.[23] ZF nanoparticles were synthesized by dissolving zinc nitrate hexahydrate and ferric nitrate nonahydrate in various volumes of bael pulp.[24] These nanoparticles, with an energy bandgap of 2.36 eV, showed strong antimicrobial activity, electrochemical sensing properties and enhanced removal efficiency for methylene blue up to 96% with photocatalytic activity under visible light. ZF nanoparticles with an average crystallite size of 4 nm were prepared from zinc acetate, iron acetate and *Brassica napus* oil using an ultrasonic cavitation method.[25] A mixture of zinc nitrate and ferric nitrate along with *Limonia acidissima* and water, when irradiated in a microwave oven for 15 min and calcined at 600°C, resulted in ZF nanoparticles with an average crystallite size of 27 nm.[26] These nanoparticles were used in the photodegradation of Evans blue and methylene blue dyes under visible radiation and showed antibacterial activity against foodborne pathogens. Extract of *Aegle marmelos* was added to an aqueous solution of zinc nitrate and ferric nitrate, and this mixture when stirred and later calcined led to the formation of ZF nanoparticles which showed antibacterial activity against gram-positive bacteria *Escherichia coli* and *Pseudomonas aeruginosa* and gram-negative bacteria *Staphylococcus aureus* and *Bacillus subtilis*, and achieved 95% drug delivery of

carfilzomib, a cancer drug.[27] Ferrous sulfate solution in alkaline medium of 10% $NH_3.H_2O$ when mixed with pure extract of *Petroselinum crispum* and stirred until reaching pH > 9 resulted in ZF nanoparticles of 100 nm.[28] Suspension of these nanoparticles in various concentrations of 10^{-3} and 10^{-5} M enhanced the germination rate and cell viability of wheat *Triticum vulgare* up to 23%.[28] Extract of stirred aqueous solution of *Piper nigrum* powder in water, when mixed and stirred with zinc nitrate hexahydrate and hydrated ferric nitrate and further heatied at 120°C in an autoclave followed by microwave exposure for 15 min, led to the formation of ZF nanoparticles of 60–80 nm which were utilized in effective photocatalytic degradation of methylene blue in visible light.[29] Extract of *Ginkgo biloba* leaves at pH of 8.0 dissolved in a saturated aqueous solution of zinc nitrate hexahydrate $[Zn(NO_3)_2.6H_2O]$ and iron nitrate nonahydrate $[Fe(NO_3)_3.9H_2O]$ stirred at a constant temperature led to the formation of ZF nanoparticles with a diameter of 12.6 nm estimated from W-H plots, and these nanoparticles were used for wastewater treatment.[30] ZF nanoparticles with crystallite size of 11–15 nm used for hyperthermia applications were prepared using magnetically stirred homogeneous extract of *Allium cepa* mixed with zinc nitrate hexahydrate $[Zn(NO_3)_2.6H_2O]$ and iron nitrate nonahydrate $[Fe(NO_3)_3.9H_2O]$ and calcined at 900°C.[31] The average size of the ZF nanoparticles was found to increase with the increase in the calcination temperature from 400 to 900°C.[32] The particle size of ZF nanoparticles was found to increase with a reduction of microstrain of ZF nanoparticles at 300°C, 500°C[33] and 900°C[34] estimated by the Debye–Scherrer and Williamson-Hall (W-H) plot methods. MFe_2O_4 (where M=Zn, Ni and Cu) nanoparticles with crystallite sizes ranging from 15 nm to 66 nm were prepared using extract of *Aloe vera* plant mixed with metal nitrates and iron nitrate and calcined from 600 to 900°C.[35] The crystallite sizes of all obtained samples increased with the increase in calcination temperature. The diverse preparation methods and different calcination temperatures and exposure times resulted in ZF nanoparticles of varying crystallite size, energy bandgap and microstrain.[36,37] We synthesized ZF nanoparticles using a simple, safe, nontoxic, eco-friendly and cost-effective green route in order to encourage sustainable processes,[38] as chemical and physical techniques are costlier, use toxic chemicals and are harmful to the environment. Extract of lemon juice mixed in a saturated solution of zinc nitrate and iron nitrate was utilized for the synthesis of the ZF nanoparticles. The structural, morphological and optical properties of the obtained nanoparticles calcined at different temperatures were investigated by synchrotron x-ray diffraction (S-XRD), field emission scanning electron microscopy (FE-SEM) and UV–visible diffuse reflectance spectroscopy (UV-Vis-DRS), respectively.

Experimental Details

Zinc nitrate hexahydrate [$Zn(NO_3)_2.6H_2O$] and iron nitrate nonahydrate [$Fe(NO_3)_3.9H_2O$] were taken in their stoichiometric ratios and dissolved in an adequate amount of water to prepare ZF nanoparticles using a sol–gel auto-combustion method. The reducing agent, primarily citric acid present in lemon juice, was used as fuel for auto-combustion. Aqueous solutions of zinc nitrate and iron nitrate were prepared separately and heated on a magnetic stirrer for 5 min at 40°C, and then both were mixed with the lemon juice. This mixture was heated at 85°C on a magnetic stirrer until combustion took place, and then dry ZF nanomaterial was obtained as shown in Fig. 1. The as-synthesized ZF nanomaterial was sintered at 100°C in a muffle furnace for 4 h to remove any moisture content and then further sintered for 4 h at varying calcination temperatures of 350°C, 550°C, 750°C and 1000°C in order to obtain ZF nanoparticles of varying particle size and energy bandgap values. Synchrotron radiation with a wavelength of 0.49 nm from the S-XRD (Beamline-11) of the Raja Ramanna Centre for Advanced Technology, Indore, India, was utilized to characterize these ZF samples, and the obtained S-XRD data (see supplementary Figure S1) were converted to Cu-Kα range to compare the results with the available JCPDS files as shown in Fig. 2. The converted S-XRD data were used to compute the crystallite size and microstrain. UV-visible diffuse reflectance spectroscopy (UV-Vis-DRS) was used to obtain the optical absorption spectrum in a wavelength region from 200 nm to 800 nm for ZF nanoparticles synthesized at four different calcination temperatures of 350°C, 550°C, 750°C and 1000°C.

Field emission scanning electron microscopy (FE-SEM) investigations were performed by dissolving and sonicating ZF nanoparticles in isopropyl alcohol (IPA) for 15 min for proper mixing, and this homogeneous solution was spread over a Si-wafer and sputtered by Cr and then finally fastened on carbon black paper to adhere on the sample holder which was scanned by FE-SEM (Carl Zeiss, model).

Results and Discussion

S-XRD profiles converted to a Cu-Kα range of ZF nanomaterials at calcination temperatures of 350°C, 550°C, 750°C and 1000°C are shown in Fig. 2. The phase of ZF nanomaterial with a trace of ZnO at ~ 32° was found with varying crystallite sizes at different calcination temperatures, and the obtained results were found to be similar to those previously reported. [26 39 40 41]

The crystallite sizes were calculated from the full width at half maximum (FWHM) of the intense diffraction peaks using the Scherrer[42] formula (1) as follows:

$$D = k\frac{\lambda}{\beta \cos\theta} \tag{1}$$

Here, $D=$ the crystallite size (nm), $k=$ shape function $=0.9$, $\lambda=$ x-ray wavelength, $\theta=$ angle of diffraction and $\beta=$ FWHM of the considered peak. The calculated crystallites sizes of various samples are plotted with the calcination temperature in Fig. 3 and are shown in Table I. An increase in crystallite size with increased calcination temperature was noted.

The crystallite size and tensile microstrain at different calcination temperatures were also estimated from the more precise W-H plot method.[43] Peak broadening appears because of the crystallite size effect ($k\lambda/(D\cos\theta)$) and self-prompted microstrain ($4\varepsilon \tan\theta$), where ε is microstrain, and the other parameters have their usual meaning as discussed above.[33] W-H plots were constructed from the following equation:

$$\beta\cos\theta = k\frac{\lambda}{D} + 4\varepsilon\sin\theta \tag{2}$$

$\beta \cos\theta$ versus $4 \sin\theta$ is plotted in Fig. 4. The intercept of Eq. 2 on the y-axis gives the average crystallite size, and the slope of the fitted straight line fixes the nonuniform tensile microstrain. The value of inhomogeneous tensile
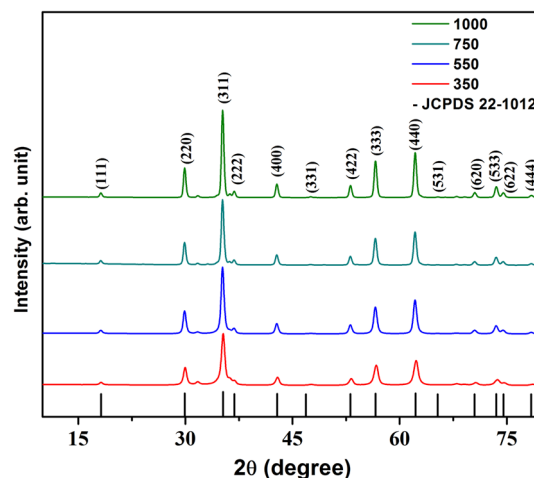
Fig. 2 XRD pattern of ZF nanoparticles synthesized through green route at different calcination temperatures (Color figure online).

Fig. 1 Block diagram for synthesis of ZF nanomaterial.

microstrain decreases with the increase in calcination temperature, which is consistent with the values of 1.49×10^{-3} and 1.00×10^{-3} for ZF nanoparticles synthesized by the co-precipitation method and at relatively different calcination temperatures of 300°C and 500°C, respectively, as reported by Singh,[33] and this was due to the substitution of lower-ionic-radius Zn^{2+} by higher-ionic-radius Fe^{2+} at tetrahedral sites.

The values of crystallite size and inhomogeneous tensile microstrain obtained from Fig. 4 and Eq. 2 for all four samples are shown in Fig. 5. The crystallite size is found to increase with an increase in calcination temperature, as higher temperature produces zinc or oxygen defects at grain boundaries, which leads to merging of ZF nanoparticles due to coalescence.[44] Inhomogeneous tensile microstrain decreases with an increase in temperature because surface effects dominate due to smaller particle size and larger surface area.[33] The values of microstrain reported here are in relative agreement with the literature,[31 33 36] as the reducing agents and the calcination temperatures of the ZF nanoparticles were different.
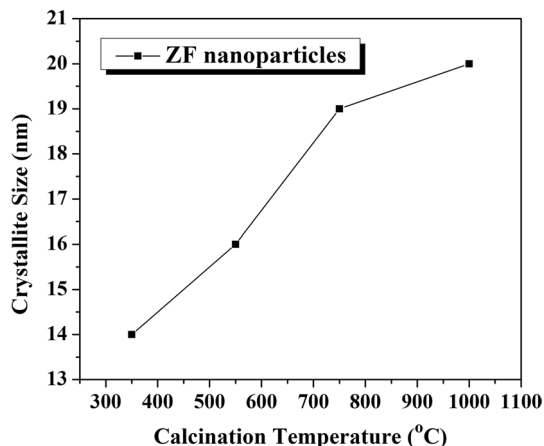
Fig. 3 Crystallite size of ZF nanoparticles versus calcination temperature.

Field Emission Scanning Electron Microscopy (FE-SEM)

The micrographs obtained by FE-SEM for the four samples of ZF nanoparticles calcined at 350°C, 550°C, 750°C and 1000°C are shown in Fig. 6, in which spherical agglomerated nanoparticles are visualized for all cases. The particle size was estimated from the micrographs using ImageJ software, and the particle size distribution is shown in Fig. 7. The particle size increased with the increase in calcination temperature.

UV-Visible Diffuse Reflectance Spectroscopy (UV-Vis-DRS)

The optical bandgap was investigated using UV-Vis-DRS. The acquired UV-Vis-DRS spectrum was converted to equivalent absorption spectrum by employing the Kubelka–Munk function as follows [45];

$$F(R) = \frac{\alpha}{S} = \frac{(1-R)^2}{2R} \tag{3}$$

where $F(R)$ = Kubelka–Munk function, $R = (R_{sample}/R_{standard})$, R_{sample} = diffuse reflectance of the sample and $R_{standard}$ = diffuse reflectance of the standard, α = absorption coefficient and S = scattering coefficient. Figure 8 shows the Kubelka–Munk function with respect to wavelength for ZF nanoparticles at different calcination temperatures. The Kubelka–Munk function $F(R)$ is proportional to the absorption coefficient (α) as follows:

$$F(R) \propto \alpha \propto \frac{\left(h\nu - E_g\right)^{\frac{1}{n}}}{h\nu} \tag{4}$$

$$(\alpha h\nu)^n \propto \left(h\nu - E_g\right) \tag{5}$$

In the above equation, $n = 2$ for direct-bandgap transition, whereas $n = 1/2$ for indirect-bandgap transitions. Here, $n = 2$ is taken to find the optical energy bandgap of ZF, as it was selected as the direct-bandgap material.[46] The absorption

Table I Data obtained from XRD analysis, UV-Vis DRS spectroscopy and FE-SEM

SN	Calcination temperature (°C)	D (from Scherrer formula in nm)	D (from W-H plot in nm)	Lattice parameter (Å)	Inhomogeneous tensile microstrain	Optical bandgap in eV (from UV-Vis-DRS)	Particle size (from FE-SEM in nm)
1	350	14	16	8.4283	0.913×10^{-3}	2.265	51
2	550	16	17	8.4492	0.213×10^{-3}	2.251	54
3	750	19	20	8.4494	0.374×10^{-4}	2.245	57
4	1000	20	21	8.4454	0.154×10^{-4}	2.225	61
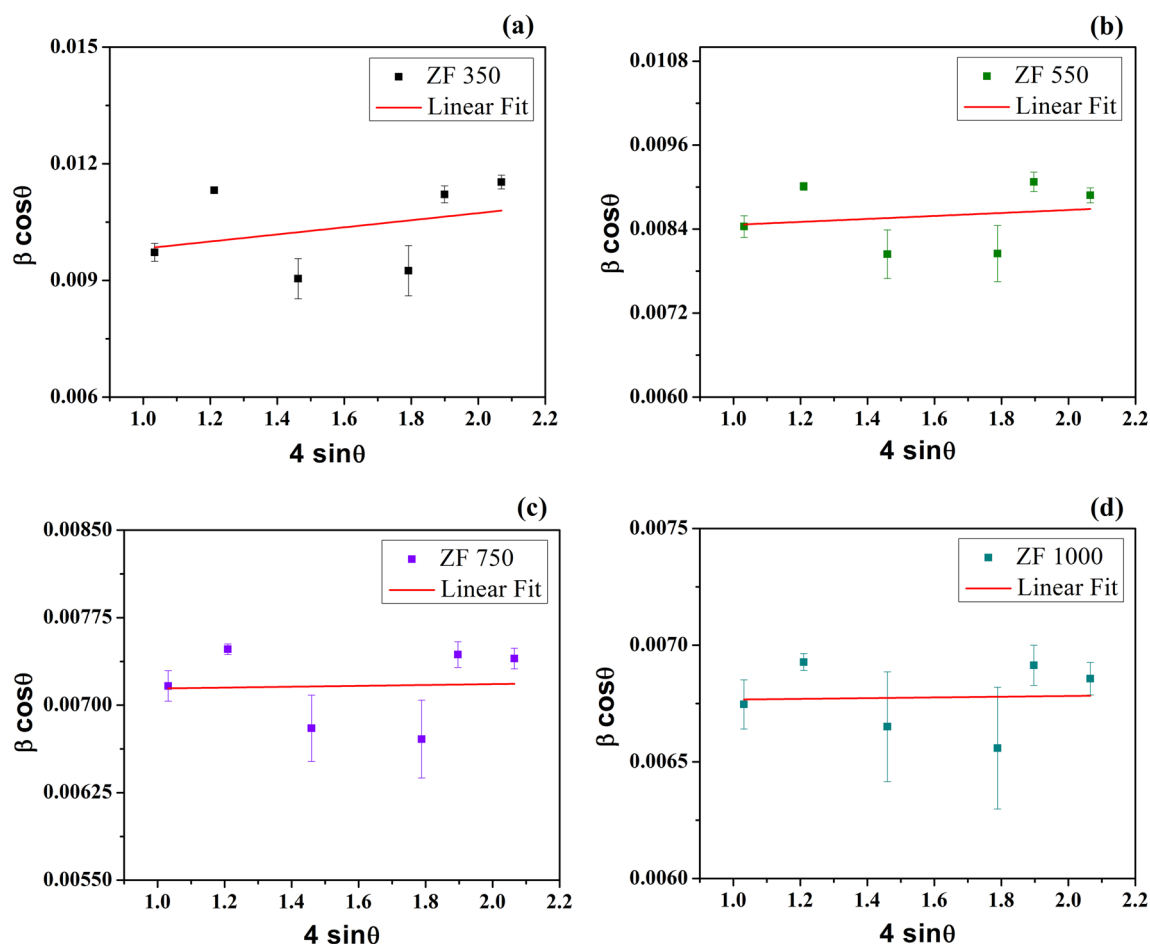
Fig. 4 W-H plot of ZF nanoparticles synthesized via a green route at calcination temperature of (a) 350°C, (b) 550°C, (c) 750°C and (d) 1000°C.
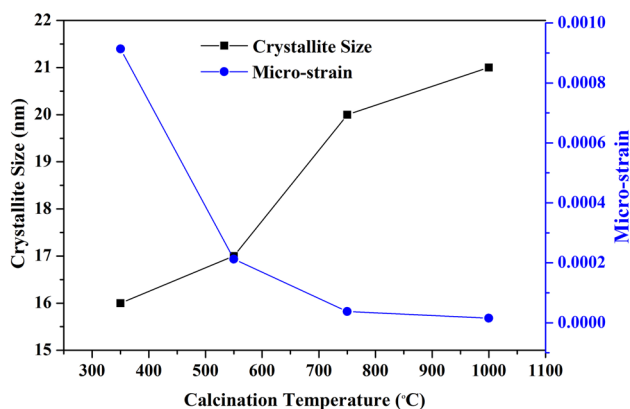
Fig. 5 Crystallite size and microstrain from W-H plot versus calcination temperature.

coefficient (α) is changed into the Tauc equation as indicated in the insets of Fig. 8.

The intersection point on the energy axis of linear fitting from the Tauc equation, [47, 48, 49] as shown in the inset of Fig. 8, results in the optical energy bandgap values. The obtained optical energy bandgap decreases with an increase in calcination temperature, as shown in Fig. 9. The value obtained for ZF nanoparticles is 2.251 eV at 550°C, which closely agrees with the value of 2.2 eV at 600°C reported in the literature.[50]

The optical absorption of nanomaterials depends on quantum confinement effects, leading to an increase in the optical energy bandgap with a reduction in crystallite size, and on surface effects, which result in a decrease in the optical energy bandgap with the reduction in crystallite size.[51] Taking the quantum confinement effects into account, the optical energy bandgap of nanomaterials can be given by the following equation[52];

$$E_{g(\text{nanomat.})} = E_{g(\text{bulk})} + \frac{h^2}{8r^2}\left(\frac{1}{m_e^*} + \frac{1}{m_h^*}\right) - 0.24 E_{\text{RY}}^* \quad (6)$$

Here, $E_{g(\text{bulk})}$ is the optical energy bandgap of the bulk, E_{RY}^* is the bulk excitation energy, h is Planck's constant, r is the radius of the crystallite, and m_e^* and m_h^* are the effective
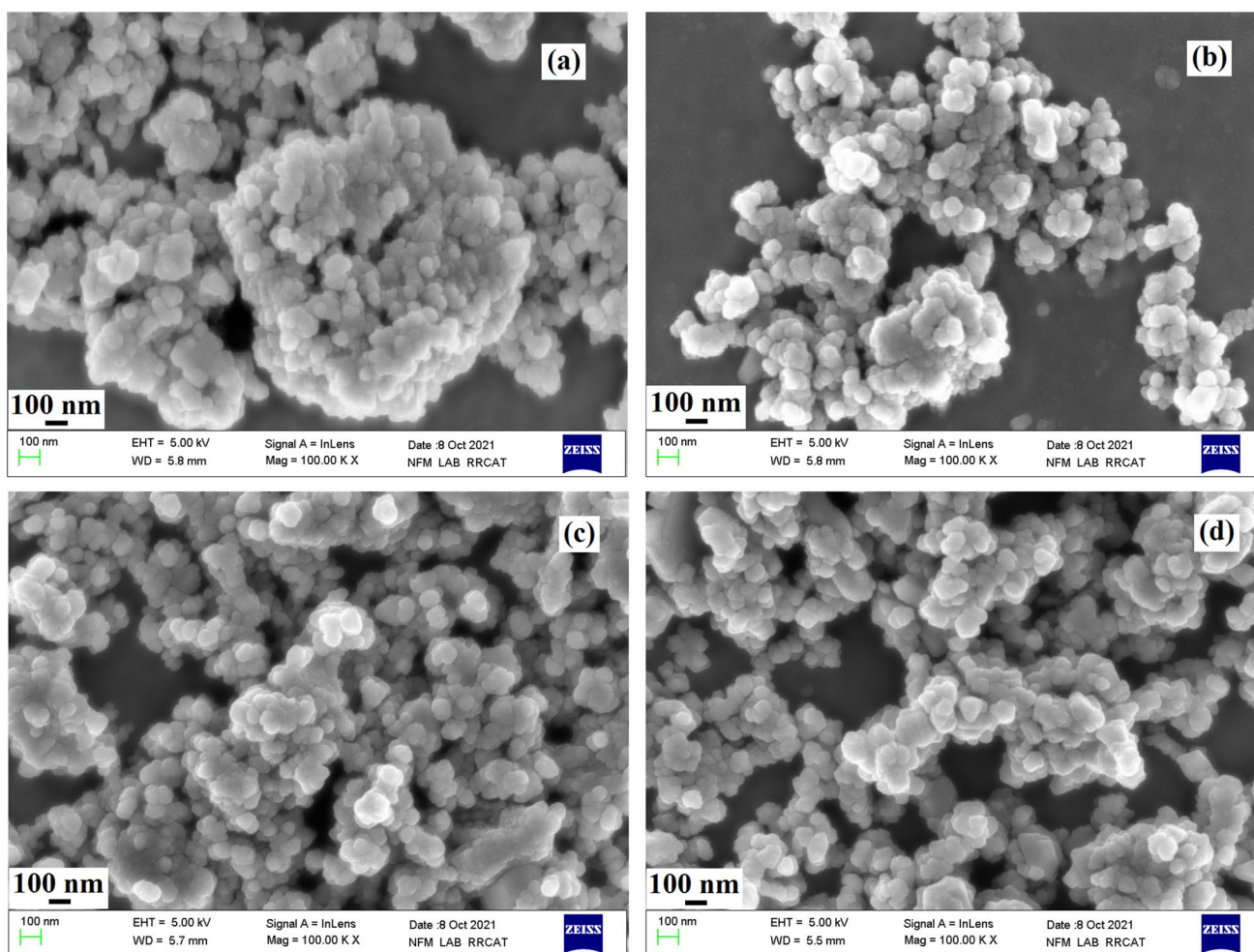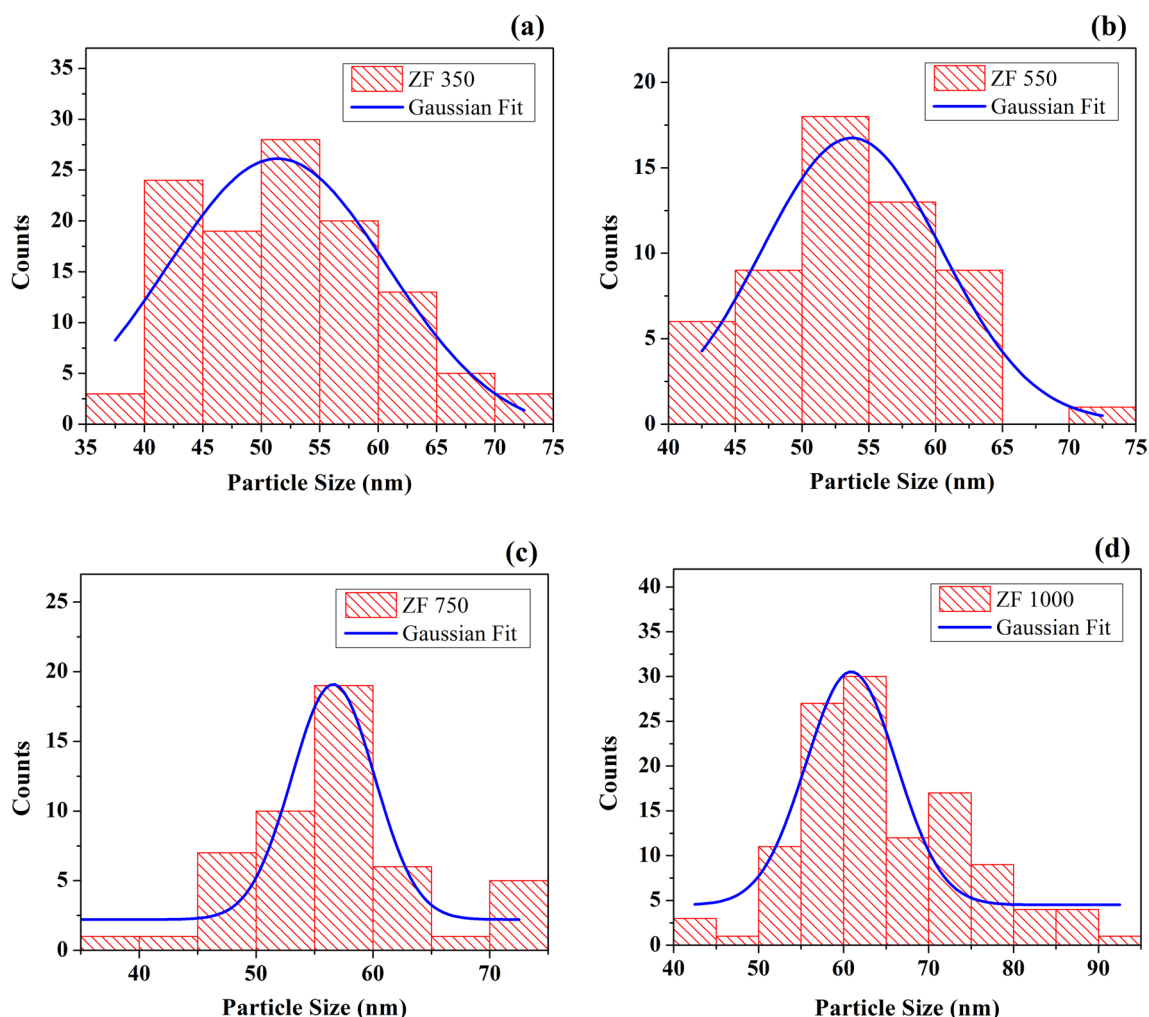
Fig. 6 FE-SEM micrographs of ZF nanoparticles at calcination temperatures of (a) 350°C, (b) 550°C, (c) 750°C and (d) 1000°C.

mass of electrons and holes, respectively. $E_{g(\text{nanomat.})}$ with respect to $\frac{1}{r^2}$ is plotted in Fig. 10, and a second-order polynomial is fitted, as it is not possible to fit the straight line, which confirms that the quantum confinement is absent.[46] The bandgap of the system is primarily derived from Fe 3d eg and t2g levels (transitions between d-d levels). The separation between d levels is a function of the intensity of the crystalline field surrounding the ion. The bandgap is modified toward greater or lower energy values with the increase or decrease in the crystalline field, respectively. Therefore, the variation in bandgap is directly related to the local distortions in the ordered average crystal lattice. When the material is annealed at different temperatures, it modifies the local distortions in the ordered average crystal lattice. This is directly reflected in the microstrain parameter. These distortions produce a change in the hybridization of metal 3d with O 2p levels or intensity of the crystalline field surrounding the ion, which mirrors the change in the bandgap.

The average crystallite size from Eq. 1, W-H plot, lattice parameter, tensile microstrain, optical bandgap from UV-Vis-DRS and particle size obtained from FE-SEM at different calcination temperatures are summarized in Table I.

It is clear from the table that both the crystallite size and the particle size of the ZF nanoparticles synthesized via the green route increased with the increase in calcination temperature, while the inhomogeneous tensile microstrain and optical bandgap decreased with the increase in calcination temperature, which is consistent with the literature. [20, 31, 33, 50]

Fig. 7 Particle size distribution for ZF nanoparticles at calcination temperatures of (a) 350°C, (b) 550°C, (c) 750°C and (d) 1000°C.

Conclusion

The S-XRD measurements demonstrate the presence of cubic phase of ZF nanoparticles synthesized at calcination temperatures of 350°C, 550°C, 750°C and 1000°C via a green route utilizing lemon juice as a fuel and reducing agent. The average crystallite size of ZF nanoparticles obtained from both Scherrer and W-H plots increased with the increase in calcination temperature, while the inhomogeneous tensile microstrain was found to decrease with increasing calcination temperature. Agglomerated particles were seen in the micrographs obtained from FE-SEM images. The optical bandgap obtained from Tauc plots by employing UV-Vis-DRS spectroscopy decreased with the increase in calcination temperature as a result of the increase in crystallite size obtained from S-XRD measurements. The small variation in the bandgap of this system is due to confined distortions in the ordered average crystal lattice as seen in the microstrain parameter, which results in hybridization of metal 3d with O 2p levels, leading to a change in the bandgap, and not because of quantum confinement.
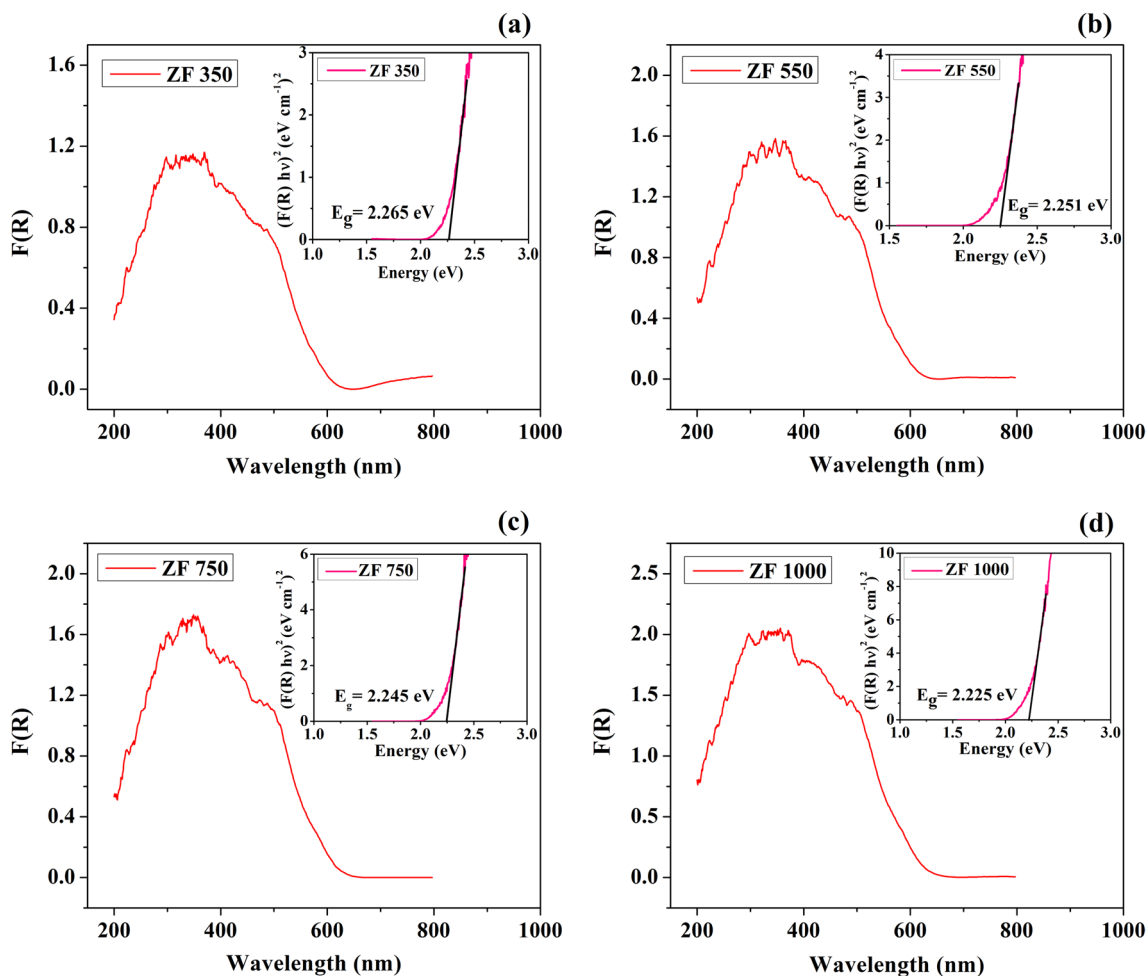
Fig. 8 Kubelka–Munk function versus wavelength at calcination temperatures of (a) 350°C, (b) 550°C, (c) 750°C and (d) 1000°C for determination of the bandgap using the Tauc equation (inset).
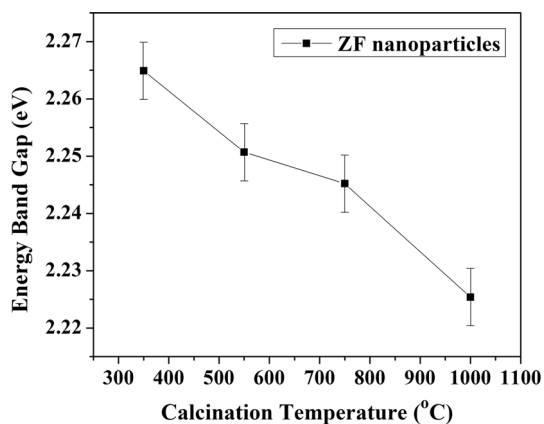

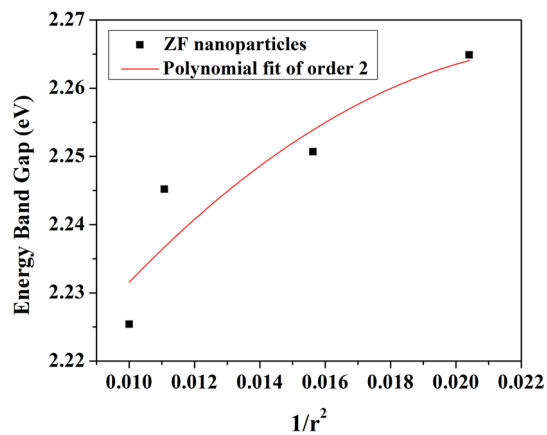**Fig. 9** Optical bandgap versus calcination temperature.

Fig. 10 $E_{g(nanomat.)}$ versus $\frac{1}{r^2}$.

References

1. S.R. Patade, D.D. Andhare, S.B. Somvanshi, S.A. Jadhav, M.V. Khedkar, and K.M. Jadhav, Self-Heating Evaluation of Superparamagnetic $MnFe_2O_4$ Nanoparticles for Magnetic Fluid Hyperthermia Application towards Cancer Treatment. *Ceram. Int.* 46, 25576 (2020).

2. A.V. Humbe, J.S. Kounsalye, S.B. Somvanshi, A. Kumar, and K.M. Jadhav, Cation Distribution, Magnetic and Hyperfine Interaction Studies of Ni-Zn Spinel Ferrites: Role of Jahn Teller Ion (Cu^{2+}) Substitution. *Mater. Adv.* 1, 880 (2020).

3. T. Pannaparayil, S. Komarneni, R. Marande, and M. Zadarko, *Subdomain* Zinc Ferrite Particles: Synthesis and Characterization. *J. Appl. Phys.* 67, 5509 (1990).

4. S.A. Jadhav, S.B. Somvanshi, M.V. Khedkar, S.R. Patade, and K.M. Jadhav, Magneto-Structural and Photocatalytic Behavior of Mixed Ni-Zn Nano-Spinel Ferrites: Visible Light-Enabled Active Photodegradation of Rhodamine B. *J. Mater. Sci. Mater. Electron.* 31, 11352 (2020).

5. M. Liang, H. Xu, and K. Xie, Bench-Scale Testing of Zinc Ferrite Sorbent for Hot Gas Clean-Up. *J. Nat. Gas Chem.* 16, 204 (2007).

6. Raghvendra Singh Yadav, Ivo Kuritka, and Jarmila Vilcakova, *Advanced Spinel Ferrite Nanocomposites for Electromagnetic Interference Shielding Applications* (Elsevier, 2020).

7. N.M. Mahmoodi and Zinc Ferrite Nanoparticle as a Magnetic Catalyst: Synthesis and Dye Degradation. *Mater. Res. Bull.* 48, 4255 (2013).

8. S.B. Somvanshi, P.B. Kharat, M.V. Khedkar, and K.M. Jadhav, Hydrophobic to Hydrophilic Surface Transformation of Nano-Scale Zinc Ferrite via Oleic Acid Coating: Magnetic Hyperthermia Study towards Biomedical Applications. *Ceram. Int.* 46, 7642 (2020).

9. S.B. Somvanshi, P.B. Kharat, T.S. Saraf, S.B. Somwanshi, S.B. Shejul, and K.M. Jadhav, Multifunctional Nano-Magnetic Particles Assisted Viral RNA-Extraction Protocol for Potential Detection of COVID-19. *Mater. Res. Innov.* 25, 169 (2021).

10. D. Maiti, A. Saha, and P.S. Devi, Surface Modified Multifunctional $ZnFe_2O_4$ Nanoparticles for Hydrophobic and Hydrophilic Anti-Cancer Drug Molecule Loading. *Phys. Chem. Chem. Phys.* 18, 1439 (2016).

11. O. Akhavan, A. Meidanchi, E. Ghaderi, and S. Khoei, Zinc Ferrite Spinel-Graphene in Magneto-Photothermal Therapy of Cancer. *J. Mater. Chem. B* 2, 3306 (2014).

12. A. Kmita, A. Pribulova, M. Holtzer, P. Futas, and A. Roczniak, Use of Specific Properties of Zinc Ferrite in Innovative Technologies. *Arch. Metall. Mater.* 61, 2141 (2016).

13. M. Bohra, V. Alman, and R. Arras, Nanostructured $ZnFe_2O_4$: An Exotic Energy Material. *Nanomaterials* 11, 1286 (2021).

14. Pushpendra Kumar, Pawan Mishra, and Sanjay Kumar Sahu, Synthesis of Ni-Zn Ferrites Using Low Temperature Sol-Gel Process. Int. J. Sci. Eng. Res. 2 (2011)

15. H. Liu, Y. Guo, Y. Zhang, F. Wu, Y. Liu, and D. Zhang, Synthesis and Properties of $ZnFe_2O_4$ Replica with Biological Hierarchical Structure. *Mater. Sci. Eng. B* 178, 1057 (2013).

16. Z. Jiao, M.Q. Li, L.F. Bian, J.H. Liu, and Y.T. Qian, The Preparation of Nano $ZnFe_2O_4$ by Spraying Coprecipitation and Its Structure Analysis. *Chin. J. Inorg. Chem.* 17, 631 (2001).

17. H. Xu, B.W. Zeiger, and K.S. Suslick, Sonochemical Synthesis of Nanomaterials. *Chem. Soc. Rev.* 42, 2555 (2013).

18. F.A. Jumeri, H.N. Lim, S.N. Ariffin, N.M. Huang, P.S. Teo, S.O. Fatin, C.H. Chia, and I. Harrison, Microwave Synthesis of Magnetically Separable $ZnFe_2O_4$-Reduced Graphene Oxide for Wastewater Treatment. *Ceram. Int.* 40, 7057 (2014).

19. I. Halikia and E. Milona, Kinetic Study of the Solid State Reaction between Alpha-Fe_2O_3 and ZnO for Zinc Ferrite Formation. *Can. Metall. Q.* 33, 99 (1994).

20. A. Bardhan, C.K. Ghosh, M.K. Mitra, G.C. Das, S. Mukherjee, and K.K. Chattopadhyay, Low Temperature Synthesis of Zinc Ferrite Nanoparticles. *Solid State Sci.* 12, 839 (2010).

21. J.P. Singh, R.C. Srivastava, H.M. Agrawal, P. Chand, and R. Kumar, Observation of Size Dependent Attributes on the Magnetic Resonance of Irradiated Zinc Ferrite Nanoparticles. *Curr. Appl. Phys.* 11, 532 (2011).

22. C.N. Chinnasamy, A. Narayanasamy, N. Ponpandian, K. Chattopadhyay, H. Guerault, and J.M. Greneche, Ferrimagnetic Ordering In Nanostructured Zinc Ferrite. *Scr. Mater.* 44, 1407 (2001).

23. N. Matinise, K. Kaviyarasu, N. Mongwaketsi, S. Khamlich, L. Kotsedi, N. Mayedwa, and M. Maaza, Green Synthesis of Novel Zinc Iron Oxide ($ZnFe_2O_4$) Nanocomposite via Moringa Oleifera Natural Extract for Electrochemical Applications. *Appl. Surf. Sci.* 446, 66 (2018).

24. V. Lakshmi Ranganatha, S. Pramila, G. Nagaraju Udayabhanu, B.S. Surendra, and C. Mallikarjunaswamy, Cost-Effective and Green Approach for the Synthesis of Zinc Ferrite Nanoparticles Using Aegle Marmelos Extract as a Fuel: Catalytic, Electrochemical, and Microbial Applications. *J. Mater. Sci. Mater. Electron.* 31, 17386 (2020).

25. M. Sivakumar, A. Towata, K. Yasui, T. Tuziuti, and Y. Iida, A New Ultrasonic Cavitation Approach for the Synthesis of Zinc Ferrite Nanocrystals. *Curr. Appl. Phys.* 6, 591 (2006).

26. M. Madhukara Naik, H.S. Bhojya Naik, G. Nagaraju, M. Vinuth, H. Raja Naika, and K. Vinu, Green Synthesis of Zinc Ferrite Nanoparticles in Limonia Acidissima Juice: Characterization and Their Application as Photocatalytic and Antibacterial Activities. *Microchem. J.* 146, 1227 (2019).

27. M. Sriramulu, D. Shukla, and S. Sumathi, Aegle Marmelos Leaves Extract Mediated Synthesis of Zinc Ferrite: Antibacterial Activity and Drug Delivery. *Mater. Res. Express* 5, 115404 (2018).

28. A.M. Korotkova, O.B. Polivanova, I.A. Gavrish, E.N. Baranova, and S.V. Lebedev, Green Synthesis of Zinc Based Nanoparticles Zinc Ferrite by Petroselinum Crispum. *IOP Conf. Ser. Earth Environ. Sci.* 341, 012175 (2019).

29. M.I. Din, S. Jabbar, J. Najeeb, R. Khalid, T. Ghaffar, M. Arshad, S.A. Khan, and S. Ali, Green Synthesis of Zinc Ferrite Nanoparticles for Photocatalysis of Methylene Blue. *Int. J. Phytoremediation* 22, 1440 (2020).

30. M. Liaskovska and T. Tatarchuk, Green Synthesis of Zinc Ferrite. *Mol. Cryst. Liq. Cryst.* 719, 45 (2021).

31. S.O. Aisida, A. Ali, O.E. Oyewande, I. Ahmad, A. Ul-Hamid, T. Zhao, M. Maaza, and F.I. Ezema, Biogenic Synthesis Enhanced Structural, Morphological, Magnetic and Optical Properties of Zinc Ferrite Nanoparticles for Moderate Hyperthermia Applications. *J. Nanoparticle Res.* 23, 47 (2021).

32. S.A. Khorrami, G. Mahmoudzadeh, S.S. Madani, and F. Gharib, Effect of Calcination Temperature on the Particle Sizes of Zinc Ferrite Prepared by a Combination of Sol-Gel Auto Combustion and Ultrasonic Irradiation Techniques. *J. Ceram. Process. Res.* 12, 504 (2011).

33. J.P. Singh, R.C. Srivastava, H.M. Agrawal, and P. Chand, Relaxation Phenomena in Nanostructured Zinc Ferrite. *Int. J. Nanosci.* 08, 523 (2009).

34. H. Basavanagoudra, R. Tanakanti, M.K. Patil, S.R. Inamdar, and K.M. Goudar, Synthesis, Characterization, and Properties of Spinel Zinc Ferrite Nanoparticles by Chemical Coprecipitation Technique. *Macromol. Symp.* 400, 2100138 (2021).

35. P. Laokul, V. Amornkitbamrung, S. Seraphin, and S. Maensiri, Characterization and Magnetic Properties of Nanocrystalline $CuFe_2O_4$, $NiFe_2O_4$, $ZnFe_2O_4$ Powders Prepared by the Aloe Vera Extract Solution. *Curr. Appl. Phys.* 11, 101 (2011).

36. M.A. Cobos, P. de la Presa, I. Llorente, A. García-Escorial, A. Hernando, and J.A. Jiménez, Effect of Preparation Methods on Magnetic Properties of Stoichiometric Zinc Ferrite. *J. Alloys Compd.* 849, 156353 (2020).

37. P. Puspitasari, U. A. Rizkia, S. Sukarni, A. A. Permanasari, A. Taufiq, and A. B. N. R. Putra, Effects of Various Sintering Conditions on the Structural and Magnetic Properties of Zinc Ferrite ($ZnFe_2O_4$). *Mater. Res.* **24** (2021)

38. X. Zhu, K. Pathakoti, and H.-M. Hwang, Green Synthesis of Titanium Dioxide and Zinc Oxide Nanoparticles and Their Usage for Antimicrobial Applications and Environmental Remediation, in *Green Synthesis, Characterization and Applications of Nanoparticles* (Elsevier, 2019), pp. 223–263

39. P.M. Prithviraj Swamy, S. Basavaraja, A. Lagashetty, N.V. Srinivas Rao, R. Nijagunappa, and A. Venkataraman, Synthesis and Characterization of Zinc Ferrite Nanoparticles Obtained by Self-Propagating Low-Temperature Combustion Method. *Bull. Mater. Sci.* 34, 1325 (2011).

40. A. Singh, A. Singh, S. Singh, P. Tandon, B.C. Yadav, and R.R. Yadav, Synthesis, Characterization and Performance of Zinc Ferrite Nanorods for Room Temperature Sensing Applications. *J. Alloys Compd.* 618, 475 (2015).

41. J.P. Singh, R.C. Srivastava, H.M. Agrawal, R.P.S. Kushwaha, P. Chand, and R. Kumar, EPR Study of Nanostructured Zinc Ferrite. *Int. J. Nanosci.* 07, 21 (2008).

42. A.L. Patterson, The Scherrer Formula for X-ray Particle Size Determination. *Phys. Rev.* 56, 978 (1939).

43. A. KhorsandZak, W.H. Abd Majid, M.E. Abrishami, and R. Yousefi, X-Ray Analysis of ZnO Nanoparticles by Williamson-Hall and Size-Strain Plot Methods. *Solid State Sci.* 13, 251 (2011).

44. Z.N. Kayani, F. Saleemi, and I. Batool, Effect of Calcination Temperature on the Properties of ZnO Nanoparticles. *Appl. Phys. A* 119, 713 (2015).

45. H. Zhu, D. Yang, G. Yu, H. Zhang, and K. Yao, A Simple Hydrothermal Route for Synthesizing SnO_2 Quantum Dots. *Nanotechnology* 17, 2386 (2006).

46. J. P. Singh, R. C. Srivastava, H. M. Agrawal, P. K. Giri, D. K. Goswami, A. Perumal, and A. Chattopadhyay, Optical Behaviour of Zinc Ferrite Nanoparticles, (2010), pp. 137–143

47. E.A. Davis and N.F. Mott, Conduction in Non-Crystalline Systems V. Conductivity, Optical Absorption and Photoconductivity in Amorphous Semiconductors. *Philos. Mag.* 22, 0903 (1970).

48. N. F. Mott and E. A. Davis, Electronic Processes in Non-Crystalline Materials, illustrate (OUP Oxford, 2012)

49. P. Jani, H. Desai, B. S. Madhukar, and A. Tanna, Investigations of Calcium Ferrite Nanoparticles Synthesized by Sol-Gel Auto Combustion and Solution Mixture Methods, *Mater. Res. Innov.* 1 (2021)

50. S.B. Patil, H.S. Bhojya Naik, G. Nagaraju, R. Viswanath, S.K. Rashmi, and M. Vijay kumar, Sugarcane Juice Mediated Eco-Friendly Synthesis of Visible Light Active Zinc Ferrite Nanoparticles: Application to Degradation of Mixed Dyes and Antibacterial Activities. *Mater. Chem. Phys.* 212, 351 (2018).

51. Y. Zhi-hao, Y. Wei, J. Jun-hui, and Z. Li-de, Optical Absorption Red Shift of Capped $ZnFe_2O_4$ Nanoparticle. *Chin. Phys. Lett.* 15, 535 (1998).

52. S.T. Tan, B.J. Chen, X.W. Sun, W.J. Fan, H.S. Kwok, X.H. Zhang, and S.J. Chua, Blueshift of Optical Band Gap in ZnO Thin Films Grown by Metal-Organic Chemical-Vapor Deposition. *J. Appl. Phys.* 98, 013505 (2005).